J Appl Electrochem (2012) 42:279–289
DOI 10.1007/s10800-012-0405-5

ORIGINAL PAPER

A study of the lithium intercalation into nanoparticles of $LiCoO_2$ from an aqueous solution

H. Heli · H. Yadegari · A. Jabbari

Received: 8 February 2012 / Accepted: 15 March 2012 / Published online: 28 March 2012

Abstract Nanoparticles of lithium cobalt oxide ($LiCoO_2$) were synthesized by means of a citrate sol–gel combustion route. The particles were characterized by scanning and transmission electron microscopies (SEM and TEM), energy-dispersive X-ray spectroscopy, and X-ray diffraction (XRD) measurements. Near spherical nanoparticles of around 100 nm were observed in SEM and TEM micrographs. XRD data indicated that the as-prepared nanoparticles presented pure phase of $LiCoO_2$ with *R*-3*m* symmetry. The kinetics of electrochemical intercalation of lithium into the nanoparticles were investigated by means of cyclic voltammetry (CV), chronoamperometry, and electrochemical impedance spectroscopy (EIS) with special emphasis on the application potential as cathode material for aqueous rechargeable lithium batteries. CV studies of the nanoparticles at slow scan rate of 0.1 mV s^{-1} between 600 and 820 mV versus Ag/AgCl, demonstrated that the nanoparticles represented well-defined reversible peaks. The nonlinear chemical diffusion of lithium into the nanoparticles was explored by EIS. In this regards, the results were discussed based on an equivalent circuit, distinguishing the kinetic properties of lithium intercalation. The kinetic parameters of lithium intercalation were obtained using the equivalent circuit, which were in good agreement with the experimental results. The changes of kinetic parameters of lithium intercalation with potential were also discussed in detail.

Keywords Lithium cobalt oxide · Intercalation · Nanoparticles · Kinetic analysis

H. Heli (✉)
Laboratory of Analytical and Physical Electrochemistry, Department of Chemistry, Science and Research Branch, Islamic Azad University, Fars 7348113111, Iran
e-mail: hheli7@yahoo.com

H. Yadegari · A. Jabbari
Department of Chemistry, K. N. Toosi University of Technology, Tehran, Iran

1 Introduction

Study of ion intercalation process is attracted much attention due to its basic role in the energy storage systems and electrochromic windows. Ion intercalation process is driven by a charge transport process from the intercalating species into a layered host compound followed by an electron transfer reaction. Intercalation and equilibration processes comprise a number of coupled steps involving great changes in the host material including a wide variation in electronic properties. Understanding the physico-chemical properties of these processes stands as a scientific task and is relevant for improving the performance of the electrochemical devices as well as designing new applications.

Traditional lithium batteries suffer from a variety of factors including cost (due to the special cell manufacturing and the costly electrode materials and nonaqueous electrolytes), safety, reactivity of the electrode materials with the nonaqueous electrolytes, performance and environmental friendliness. Furthermore, nonaqueous electrolytes usually have ion conductivities about two orders of magnitude lower than aqueous electrolytes. The salts and separators used in commercial lithium-ion cells are expensive as well. These disadvantages urge the development of less expensive and environmentally friend energy-storage devices, such as rechargeable lithium-ion batteries with an aqueous electrolyte [1–4] and aqueous hybrid supercapacitors [5].

Recent studies have been shown that nanosized materials represent high surface energy and ion intercalation capacity [6, 7]. These nanostructured materials have small depths and short channels for the ion intercalation. These properties cause excellent electrochemical performance in terms of cyclability and specific capacity [6]. On the other hand, nanostructured materials have many sub-band gap energy states between the valence and conduction bands which originate from the surface defects. Electrochemical lithium intercalation occurs via electron injection into these sub-band-gap energy states to maintain the electroneutrality [8]. It causes a regular change in the Fermi-energy level without enduring significant structural changes and therefore, a flat discharge curve [9].

$LiCoO_2$ has emerged as an interesting material for rechargeable lithium batteries due to its relatively high specific capacity, high energy density, long cycle life, and reasonably good safety characteristics [10]. The main investigations were mainly on the synthesis of this oxide using various methods such as sol–gel [11], spray pyrolysis [12], co-precipitation process [13], and freeze drying [14]. The electrochemical properties of $LiCoO_2$ were also studied in nonaqueous solutions [15, 16]. Some other researches designed rechargeable lithium batteries based on this material using aqueous solutions [1, 3, 17]. However, a detailed study on the intercalation of lithium ion in this oxide from an aqueous solution is lacking. The presented work refers to the synthesis of nanoparticles of $LiCoO_2$ by a citrate sol–gel method. Then, the intercalation properties of the oxide in aqueous $LiNO_3$ solution were investigated.

2 Materials and methods

2.1 Materials

All chemicals were of analytical grade from Merck and were used without further purification. All solutions were prepared with doubly distilled water.

2.2 Synthesis of nanoparticles of $LiCoO_2$

Nanoparticles of $LiCoO_2$ were synthesized by a citrate sol–gel method. The synthesis process is briefly described as follows: a solution containing stoichiometric amount of lithium acetate and cobalt(II) acetate was mixed with a solution of citric acid anhydrous under stirring. The ratio of total amount of metal ions to citric acid was 1:1. The obtained mixture was evaporated at 80 °C for 8 h until conversion to a gel. Afterward, the obtained gel was further dried in an oven at 120 °C overnight to remove the excess water. The remaining solid mass was grounded and then calcined at 500 °C for 10 h to obtain nanoparticles of $LiCoO_2$.

2.3 Electrode preparation

In order to prepare the working electrode for the electrochemical experiments, $LiCoO_2$ nanoparticles (80 %) was ground with polyvinylidene difluoride (PVDF) (10 %) and acetylene black (10 %), and dispersed in *N*-methyl pyrrolidone (NMP) by means of an ultrasonic bath to obtain a paste. The resulting composite was supported on a 2.0-mm diameter Pt disk electrode and then heated to 100 °C in an oven for several hours. The working electrode contained $\approx$0.3 mg of the active material. The thickness of the active material film was calculated from the loaded mass, density of $LiCoO_2$ and the surface area of the working electrode and was achieved to be about 4.7 μm. The electrochemical behavior of the electrode was studied in a conventional three-electrode cell with a Pt disk and an Ag/AgCl (3 M KCl) as the counter and reference electrodes, respectively. The supporting electrolyte was a 1.0 M $LiNO_3$ solution.

2.4 Instruments and apparatus

Electrochemical measurements were carried out by a μ-Autolab potentiostat/galvanostat, type III, FRA2 (The Netherlands). In impedance measurements, the frequency range of 100 kHz to 50 mHz was employed while the a.c. voltage amplitude was 10 mV and the equilibrium time was 5 s. The system was run by a PC through FRA and GPES 4.9 softwares.

Surface morphological studies were carried out using a Model X-30 Philips scanning electron microscope (SEM) with energy-dispersive X-ray spectroscopy (EDS) capability. The transmission electron microscopy (TEM) was performed using a CEM 902A ZEISS transmission electron microscope, with an accelerating voltage of 80 kV. These techniques provided information about the morphology and size of the particles. In order to prepare samples for TEM, the synthesized powder was dispersed in acetone, then a drop of this mixture was placed on a carbon-covered copper grid (400 mesh) and solvent was evaporated.

Powder X-ray diffraction (XRD) patterns were recorded by a Philips X'Pert (The Netherlands) using Cu Kα radiation at 40 kV and 30 mA in the 2θ degree range from 10° to 90°.

3 Results and discussion

3.1 Electron microscopy

Figure 1 shows SEM (a) and TEM (b) images of $LiCoO_2$ nanoparticles. Both types of images represent particles with an average size less than 100 nm. A size distribution histogram corresponds to the TEM image is also depicted in

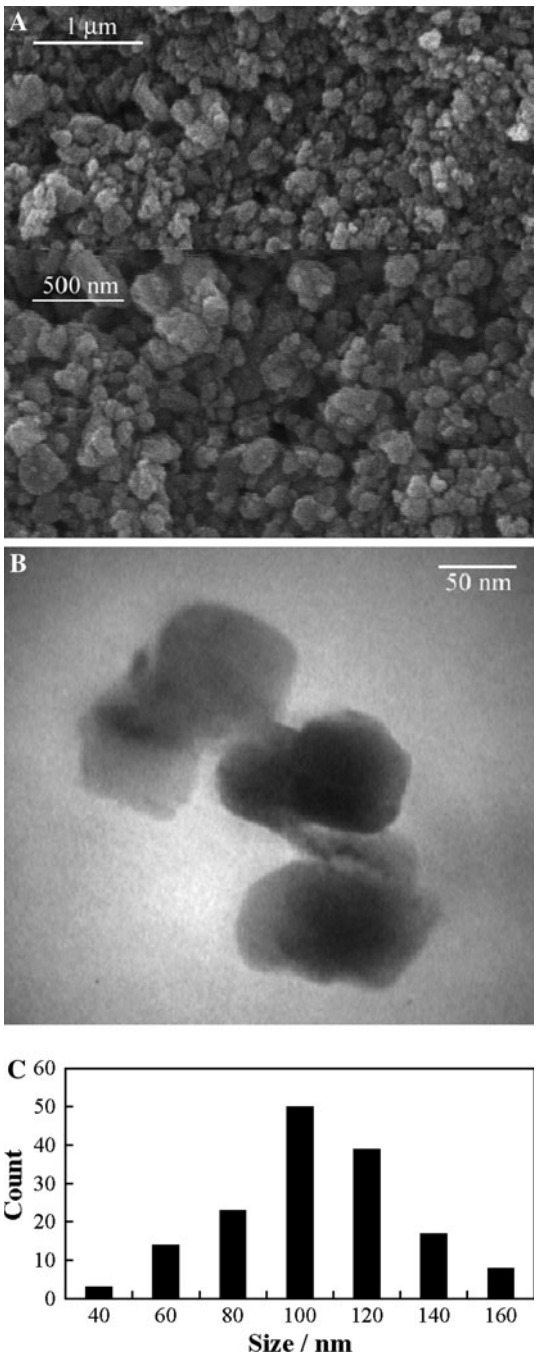

Fig. 1 SEM (**a**) and TEM (**b**) images of the $LiCoO_2$ nanoparticles and a size distribution histogram (**c**) corresponds to the TEM image

Fig. 1c. The particles are arranged in a narrow size distribution with a mean size of $\approx$100 nm.

Figure 2 shows the SEM–EDS spectrum with elemental mapping for the nanoparticles. A low magnification (large-scale area selected, without going to the morphology and size of the nanoparticles) SEM micrograph of $LiCoO_2$ nanoparticles is shown in Fig. 2a. Figure 2b, c shows the corresponding EDS elemental mapping toward Co and O elements, respectively. The elemental mappings show the uniform distribution of cobalt and oxygen atoms, which indicates the uniform formation of the $LiCoO_2$ structure. Figure 2d shows an EDS spectrum of the nanoparticles. No peak was identified due to the presence of carbon in $LiCoO_2$ nanoparticles confirming the formation of organic-free $LiCoO_2$ nanoparticles.

3.2 XRD measurement

Figure 3 represents a typical XRD pattern of as-synthesized $LiCoO_2$ nanoparticles. The pattern contains slightly broadened peaks, due to the nanometer-size effect [18]. The nanoparticles are randomly oriented polycrystalline with main diffraction peaks at 2θ values of 18.95, 37.43, and 45.28. These correspond to (0 0 3), (1 0 1), and (1 0 4) reflections, respectively. The peaks can be identified with those for a rhombohedral $LiCoO_2$ structure with *R*-3*m* space group (No. 166) [19]. The distinct splitting of (0 0 6)/(1 0 2) and (0 1 8)/(1 1 0) peaks suggests the good hexagonal ordering and superior layered characteristics. The results indicate the good crystallinity of the synthesized $LiCoO_2$ nanoparticles. The cell parameters are also obtained for the nanoparticles as $a = 2.82$ Å, $c = 14.04$ Å, $c/a = 4.98$, and $V = 96.49$ Å^3. In addition, no peak from other phases was detected indicating that the nanoparticles were of high purity.

3.3 Cyclic voltammetry

Figure 4a shows a typical cyclic voltammogram of $LiCoO_2$ nanoparticles recorded in 1.0 M $LiNO_3$ solution using a potential sweep rate of 0.1 mV s^{-1}. One pair of sharp and well-defined reversible redox peak with a mid-peak potential of 757 mV is observed in the voltammogram owning to the insertion and extraction of lithium ion into $LiCoO_2$ nanoparticles. In some other reports [1, 20, 21], in the voltammograms of the synthesized or commercial $LiCoO_2$ samples recorded in organic or aqueous solutions, multiple redox couples were observed. These multiple redox couples were attributed to the lithium ion intercalation/deintercalation following by phase transitions and volume changes. However, in the voltammogram presented here, the remarkable point is that during the intercalation/deintercalation process, nanoparticles of $LiCoO_2$ do not exhibit any phase change. In addition, in this voltammogram, the peak potential separation is 16 mV. This value is much smaller than those observed for the commercial $LiCoO_2$ samples in aqueous solutions [1, 3]. The results reveal the fact that decreasing the particles size to nanometer scale can improve the intercalation/deintercalation kinetics. The nanosized materials bear surface defects which should be fundamentally considered in comparison with the large counterparts. On the other hand, the nanosize

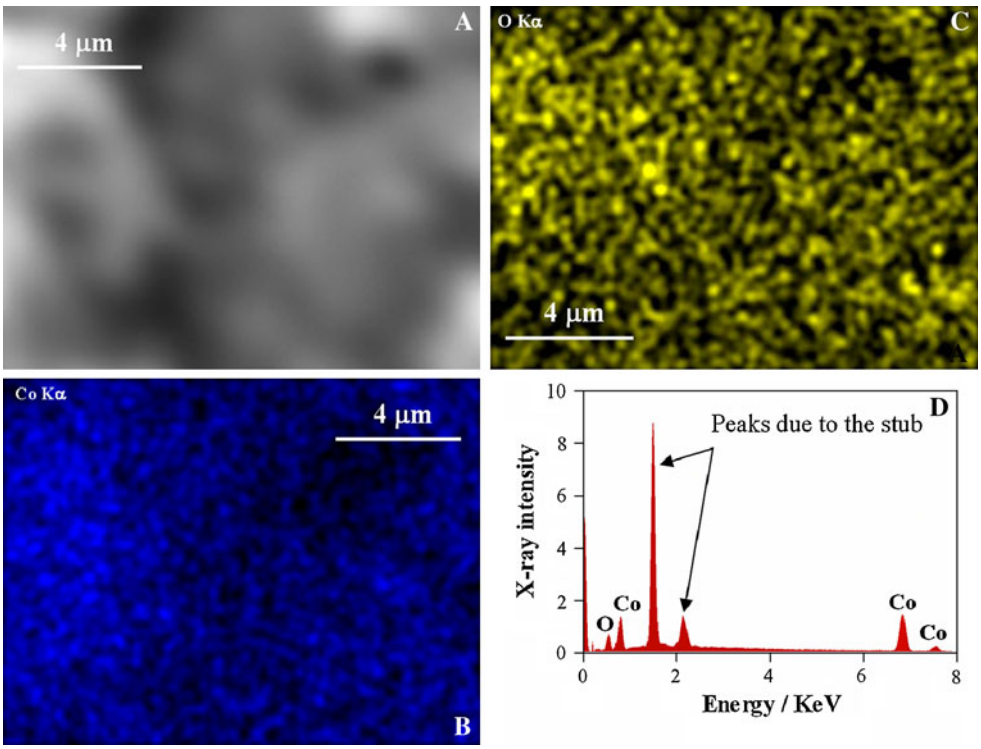

Fig. 2 A low magnification SEM image (**a**), EDS mappings of Co (**b**) and O (**c**) elements and an EDS spectrum (**d**) of the $LiCoO_2$ nanoparticles

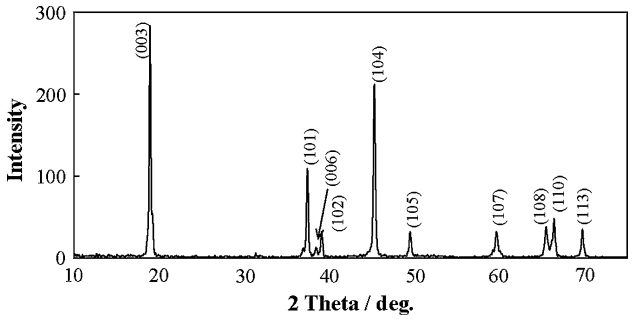

Fig. 3 A typical X-ray diffraction pattern of the $LiCoO_2$ nanoparticles

effect allows a solid-state solution behavior with a small lattice expansion; the nanosized materials represent short diffusion length and higher surface reactions make for homogeneous lattice expansion/contraction not possible with large-size materials. This strongly contrasts with the phase transition known for the large-scale oxides. Another point in the voltammogram is that the reduction peak is broader than the oxidation one, indicating that compared to the deintercalation, intercalation of lithium ion into the nanoparticles performs with lower rate. This may be due to the desolvation of lithium ions by water molecules. Moreover, 1st, 2nd, 5th, and 10th cycles of $LiCoO_2$ nanoparticles recorded in 1.0 M $LiNO_3$ solution are shown in Fig. 4b. The results indicate good cyclability of the electrode material. Finally, it should be added that no obvious changes in the voltammograms were observed using higher concentrations of the electrolyte and using other lithium salts. Lower concentrations of the electrolyte caused to depletion of the electron transfer kinetics (higher peak potential separation). Therefore, 1.0 M $LiNO_3$ solution was employed as the best electrolyte.

Figure 5 shows cyclic voltammograms of $LiCoO_2$ nanoparticles in 1.0 M $LiNO_3$ solution recorded at different potential sweep rates in the range of 2–40 mV s^{-1}. Upon increasing the potential sweep rate, the height and area of the redox peaks increase, while the corresponding charges (which correspond to the capacity of the electrode) remain almost unchanged. This further confirms the favorable kinetics of charge transfer even at high potential sweep rates. In addition, both anodic and cathodic currents linearly depend on the square root of the potential sweep rate (Fig. 5, inset). These dependencies indicate that the intercalation/deintercalation process is controlled by diffusion. From the slope of the linear dependency of the cathodic peak current on the square root of the potential sweep rate (Fig. 5, inset), and using Randles–Sevcik equation (written for a reversible electron-transfer process) [22]:

$$I_{p,c} = \left(2.69 \times 10^5\right) n^{3/2} A C^*_{Li} D^{1/2}_{Li} v^{1/2} \quad (1)$$

where $I_{p,c}$, n, A, and v are the peak current, number of exchanged electrons, surface area of the electrode, and potential sweep rate. D_{Li} is the chemical diffusion coefficient of lithium ion and C^*_{Li} is the bulk concentration of lithium ion (0.0516 mol cm^{-3} for $LiCoO_2$ derived from

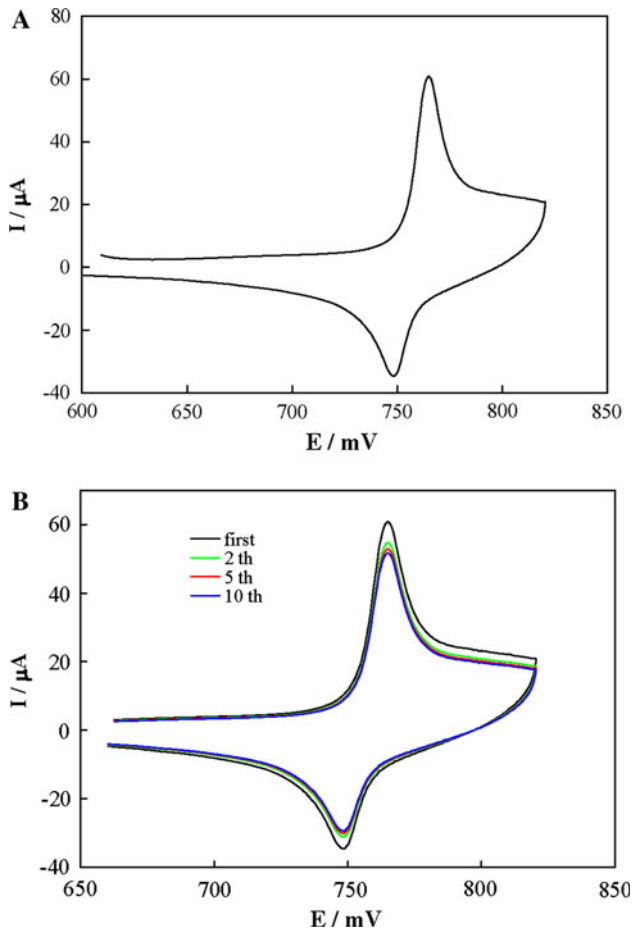

Fig. 4 **a** A typical cyclic voltammogram of $LiCoO_2$ nanoparticles recorded in 1.0 M $LiNO_3$ solution. The potential sweep rate was 0.1 mV s^{-1}. **b** The 1st, 2nd, 5th, and 10th cycles of the $LiCoO_2$ nanoparticles recorded in 1.0 M $LiNO_3$ solution. The potential sweep rate was 0.1 mV s^{-1}

theoretical density of 5.06 g cm^{-3}), D_{Li} into $LiCoO_2$ nanoparticles during the intercalation process was obtained as 1.59×10^{-10} cm^2 s^{-1}. This value is in good agreement with that reported elsewhere [1]. It should be noted that diffusion of lithium ion into the host materials is nonlinear and its value is potential dependent [23]. On the other hand, the value of the diffusion coefficient at the peak potential of cyclic voltammograms is the lowest [24, 25]. Dependency of D_{Li} on potential will be attained using chronoamperometry (CA) and impedance spectroscopy (vide infra).

3.4 Chronoamperometry

CA is a powerful electrochemical technique for characterization of ion diffusion in the solid state host materials [7, 26, 27] where the working electrode potential is stepped from an initial value which no electrolysis occurs to a final value where a species is electroreactive. The resulting

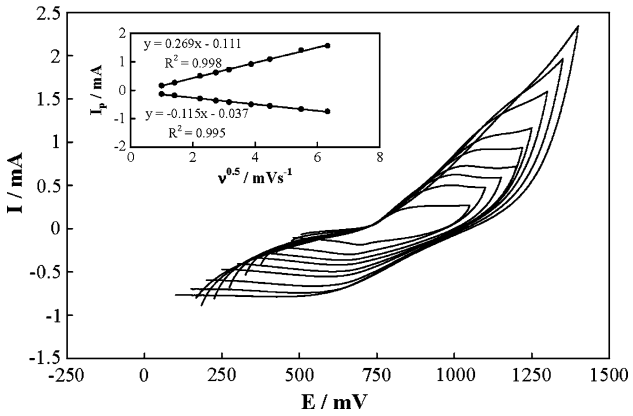

Fig. 5 Cyclic voltammograms of the $LiCoO_2$ nanoparticles in 1.0 M $LiNO_3$ solution recorded at different potential sweep rates from the inner to the outer of 2, 5, 7.5, 10, 15, 20, 30, 40, and 50 mV s^{-1}. *Inset* dependency of the cathodic and anodic peak currents on the square root of the potential sweep rate

current from faradaic processes occurring at the electrode is monitored as a function of time until steady-state conditions are achieved. The expression of the current response to a potential step at a long time domain, assuming one-dimensional diffusion transport of a species under finite-space conditions, can be represented as follows [26]:

$$I(t) = 2\Delta Q/\tau_d \sum_{m=0}^{\infty} \exp\left[-(2m-1)^2\pi^2 t/(4\tau_d)\right] \quad \text{for} \quad t > \tau_d \tag{2}$$

where $I(t)$ is the current response to the potential step, ΔQ is the total charge transferred into the electrode during the potential step, τ_d is the diffusion time constant, t is the elapsed time from the beginning of the potential step, and m is an integer number, with:

$$\tau_d = l^2/D_{Li} \tag{3}$$

and

$$\Delta Q = \int_0^{\infty} I(t)\mathrm{d}t = -FAl\Delta C \tag{4}$$

where l is the diffusion length, F is the Faraday constant, and ΔC is the variation of the diffusing species concentration. In the short time domain, however, an alternative expression for the current response is represented:

$$I(t) = \Delta Q/(\pi t\tau_d)^{1/2}\left[1 + 2\sum_{m=0}^{\infty}(-1)^m \exp\left(-m^2\tau_d/t\right)\right] \quad \text{for} \quad t < \tau_d \tag{5}$$

In the study presented here, a step potential of 740 mV (correspond to the potential of the cathodic peak in the

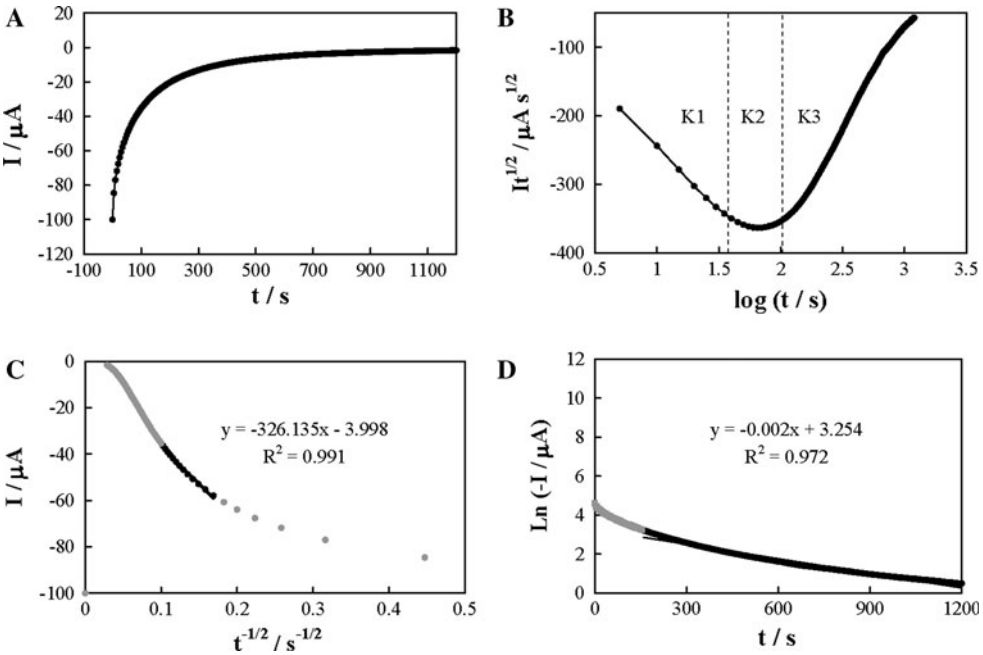

Fig. 6 **a** A typical chronoamperogram of the $LiCoO_2$ nanoparticles recorded in 1.0 M $LiNO_3$ solution using a step potential of 740 mV; **b** the corresponding Cottrell plot; **c** the corresponding I versus $t^{-1/2}$ plot; **d** the corresponding ln(I) versus t plot

cyclic voltammetry (CV) plot, Fig. 4a) was applied and the resulted chronoamperogram is depicted in Fig. 6a. Since the mass transport of lithium ion occurs only by diffusion, the net current decays exponentially to a limiting value. A diagnostic tool for identifying the kinetic behavior of lithium ion can be attained by plotting the product $I \times t^{1/2}$ versus log(t) (the Cottrell plot). The corresponding Cottrell plot (for the chronoamperogram depicted in Fig. 6a) is shown in Fig. 6b. In the plot, various time domains of the intercalation process for lithium ion into $LiCoO_2$ nanoparticles are witnessed. Three different kinetic regions can be distinguished from the plot corresponding to the separate steps of the entire intercalation process: (a) Region K1 (short term) corresponds to the interfacial charging of both the Pt substrate/$LiCoO_2$ and the $LiCoO_2$/electrolyte interfaces (i.e., double layer charging). (b) Region K2 (medium term) represents almost constant values for $It^{1/2}$, reflecting the fact that semi-infinite planar diffusion of lithium ions into $LiCoO_2$ nanoparticles occurs in this region. The following expression, which is derived from Eq. (5), is valid for region K2 [28]:

$$I(t) = D_{\mathrm{Li}}^{1/2}\Delta Q/l\pi^{1/2}t^{1/2} \tag{6}$$

where l (the diffusion length) is assumed to be equal to $LiCoO_2$ film thickness. From the slope of the I versus $t^{-1/2}$ plot in the time domain of 35–95 s which is shown in Fig. 6c, and using Eq. (6), D_{Li} into $LiCoO_2$ nanoparticles was obtained as 9.91×10^{-9} cm^2 s^{-1}. (c) Region K3 (long term) represents the finite-space diffusion of lithium ion into $LiCoO_2$ nanoparticles in the long time domain. Dependency of the response current with time in region K3 can be derived from Eq. (2) and represented by the following equation [28, 29]:

$$I = \left(2\Delta Q D_{\mathrm{Li}}/l^2\right)\exp\left(-\pi^2 D_{\mathrm{Li}}t/4l^2\right) \tag{7}$$

Figure 6d shows the plot of ln(I) versus t which has a linear relation for $t > 160$ s. From the slope of this line and using Eq. (7), D_{Li} into $LiCoO_2$ nanoparticles was obtained as 2.26×10^{-10} cm^2 s^{-1}. Interestingly, the diffusion coefficients obtained from the medium (region K2) and long (region K3) time domains are in close agreement within and with the diffusion coefficient obtained from CV technique.

3.5 Chronopotentiometry

Figure 7 shows typical chronopotentiograms (charge/discharge curves) for $LiCoO_2$ nanoparticles in 1.0 M $LiNO_3$ solution in the potential range of 650–900 mV at a C/5 rate or 32 mA g^{-1}. The charge/discharge curves show a plateau at about 750 mV, corresponding to the redox potential of the cyclic voltammogram (Fig. 4) and indicate that the lithium intercalation/deintercalation into/from $LiCoO_2$

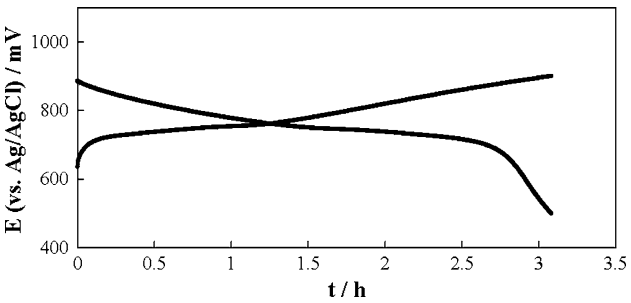

Fig. 7 Typical chronopotentiograms (charge/discharge curves) of $LiCoO_2$ nanoparticles in 1.0 M $LiNO_3$ solution in the potential range of 650–900 mV at a C/5 rate or 32 mA/g

nanoparticles is a one-step process. The discharge capacity of $LiCoO_2$ nanoparticles was achieved to be 90 mAh/g and the electrode material exhibits >95 % Columbic efficiency. This value is greater than the values, which have been reported for $LiCoO_2$ in aqueous electrolytes [4, 17].

3.6 Electrochemical impedance spectroscopy

Electrochemical impedance spectroscopy can access relaxation phenomena over many orders of magnitude and has been employed for the study of the kinetics of the charge transfer and mass transport phenomena during the intercalation process into the mainly porous electrodes [7, 30]. The processes involved in the course of lithium intercalation/deintercalation are a combination of: (a) electron injection at the host material/current collector interface, (b) diffusion of lithium ion in the solid lattice of the host material, (c) flipping–flopping of lithium ion across the host material/solution interface, and (d) the lithium ion transport in the bulk of solution [31]. It is taken into account that the ion transport in the bulk of solution is not fast enough to control the rate of the intercalation process.

Figure 8 represents Nyquist diagrams recorded at various dc-offset potentials of 650–1,100 mV correspond to the entire range of swept potential in the cyclic voltammogram represented in Fig. 4 and the whole region of charge/discharge curves depicted in Fig. 7. Appearance of different signatures in the Nyquist diagrams (denoted as responses at high, medium, and low frequencies) implies different physico-chemical processes occurred during the intercalation/deintercalation process. Also, the similarity in the patterns of the Nyquist diagrams indicates that the same electrochemical mechanism was occurred during the process in the entire range of the dc-offset potential. In the Nyquist diagrams, at high frequencies, a squashed and depressed semicircle with an approximate unit slope is appeared. At medium frequencies, a depressed semicircle (an arc) is appeared. At low frequencies, a diffusional impedance is located corresponds to the mass transport following by accumulation of intercalative lithium ion in the host material ($LiCoO_2$ nanoparticles).

The high-frequency response is attributed to the charge (electron) injection across the interface of current collector/electrode material and is related to the Co(IV)/Co(III) redox transition. This relation is further confirmed by the fact that the diameter of this semicircle (which is the charge transfer resistance of the electrodic process) highly depends to the dc-offset potential and the corresponding capacitance (which is the double layer capacitance) is high due to the charge transferring across the high surface area

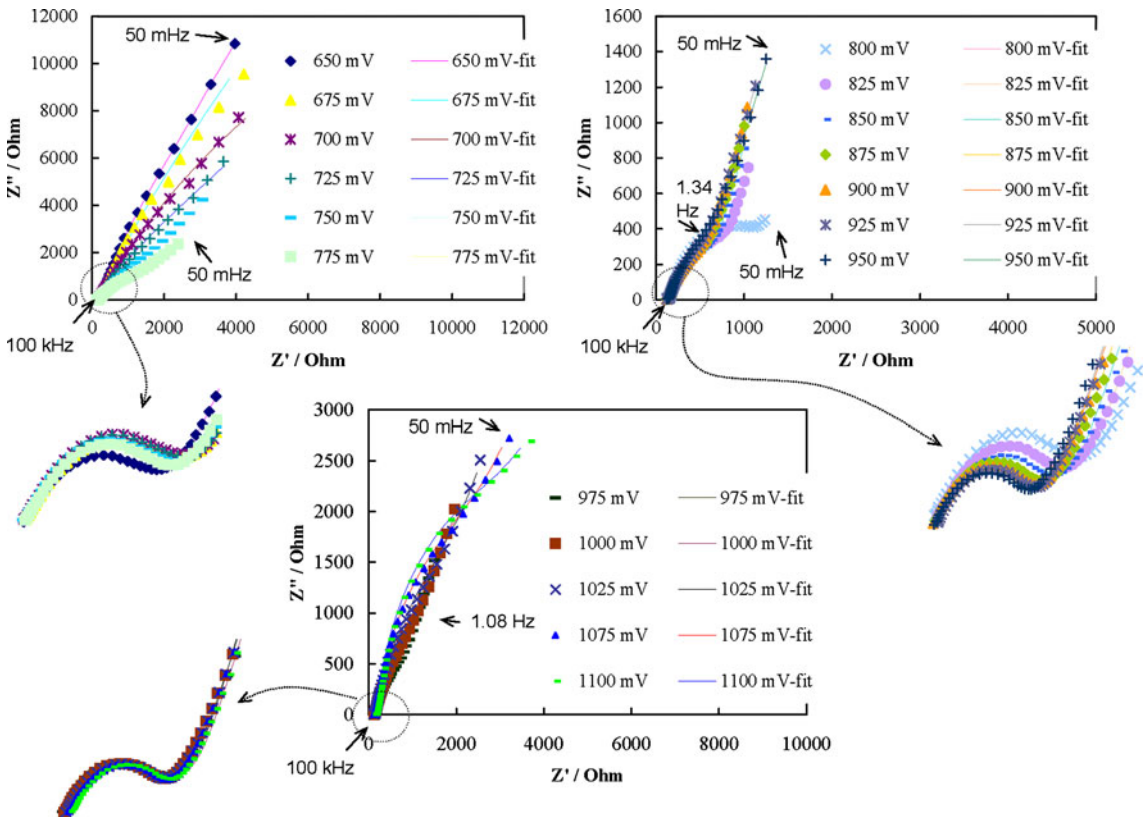

Fig. 8 Nyquist diagrams of the $LiCoO_2$ nanoparticles in 1.0 M $LiNO_3$ solution recorded at various dc-offset potentials of 650–1,100 mV

Table 1 Values of the equivalent circuit elements obtained by fitting the experimental results in the Nyquist diagrams represented in Fig. 8, the corresponding relative errors and values of the diffusion coefficient of lithium ion at different bias

Bias (mV)	R_s (Ω)	R_{ct} (Ω)	CPE_{dl}		W_o	$D_{Li} \times 10^{10}$ ($cm^2\ s^{-1}$)
			CPE_{dl}–T × 10^5 ($\Omega^{-1}\ s^{\varphi}$)	CPE_{dl}–φ	τ_D/s	
650	120.2 (0.52 %)	46.5 (1.75 %)	9.55 (7.79 %)	0.69 (1.36 %)	0.018 (7.9 %)	14.7
675	120.4 (0.5 %)	45.7 (1.79 %)	7.54 (7.90 %)	0.69 (1.34 %)	0.025 (7.7 %)	10.5
700	120.2 (0.51 %)	45.1 (1.94 %)	6.66 (8.60 %)	0.69 (1.44 %)	0.035 (6.8 %)	6.92
725	120.0 (0.52 %)	44.07 (1.92 %)	6.22 (8.76 %)	0.69 (1.44 %)	0.075 (5.9 %)	3.28
750	119.5 (0.46 %)	42.77 (1.91 %)	6.32 (8.80 %)	0.69 (1.36 %)	0.173 (5.3 %)	1.45
775	119.1 (0.48 %)	40.76 (1.76 %)	6.42 (8.26 %)	0.69 (1.43 %)	0.143 (5.3 %)	1.75
800	120.7 (0.40 %)	37.73 (1.70 %)	6.63 (8.21 %)	0.69 (1.25 %)	0.105 (5.2 %)	2.37
825	119.6 (0.43 %)	33.81 (1.72 %)	7.30 (8.54 %)	0.68 (1.27 %)	0.06 (5.1 %)	4.21
850	120.3 (0.46 %)	30.77 (1.46 %)	7.58 (7.49 %)	0.68 (1.23 %)	0.048 (5.1 %)	5.34
875	121.3 (0.52 %)	28.51 (1.46 %)	7.23 (7.66 %)	0.68 (1.37 %)	0.043 (5.1 %)	5.97
900	119.8 (0.5 %)	27.05 (1.40 %)	7.19 (7.48 %)	0.68 (1.35 %)	0.038 (5.1 %)	6.72
925	118.2 (0.51 %)	26.22 (1.55 %)	7.77 (8.24 %)	0.68 (1.16 %)	0.03 (5.3 %)	8.60
950	120.1 (0.52 %)	25.06 (1.57 %)	7.57 (8.24 %)	0.68 (1.14 %)	0.025 (5.2 %)	9.70
975	119.5 (0.46 %)	24.36 (1.35 %)	7.62 (8.31 %)	0.68 (1.12 %)	0.02 (5.3 %)	12.49
1,000	119.1 (0.48 %)	23.9 (1.33 %)	7.76 (7.17 %)	0.68 (1.23 %)	0.019 (5.2 %)	13.27
1,025	120 (0.40 %)	23.84 (1.30 %)	7.90 (7.09 %)	0.68 (1.12 %)	0.018 (5.4 %)	13.96
1,050	119.6 (0.43 %)	24.03 (1.45 %)	8.43 (6.91 %)	0.68 (1.25 %)	0.017 (5.7 %)	14.73
1,075	120.3 (0.46 %)	23.80 (1.44 %)	8.54 (7.57 %)	0.68 (1.24 %)	0.0165 (6.5 %)	15.24
1,100	120.3 (0.46 %)	23.31 (1.28 %)	8.67 (7.57 %)	0.68 (1.10 %)	0.016 (7.1 %)	15.7

of the electrode (see Table 1). This high surface area, on the other hand, can arise from the porous structure of the electrode and the rough structure at the film particle interface [24] (vide infra). In addition, it should be noted that very high-frequency semicircles observing in some studies on the lithium intercalation process for composite electrodes [32, 33]. These semicircles have been attributed to the interface parameters such as electrode porosity, surface film formed on the active material and the current collector, and/or bulk of materials, may appear at very high frequencies and were not detectable in the swept frequency range in this work. The high-frequency response can be characterized by an equivalent electrical element of the parallel combination of the charge transfer resistance and the double layer capacitance. In order to obtain a satisfactory fitting of Nyquist diagrams to an equivalent circuit, it is usually necessary to replace the capacitances with constant phase elements in the equivalent circuit. The impedance of the constant phase element is [34]:

$$Z_{CPE} = 1/T(j\omega)^{\varphi} \quad (8)$$

where T is the constant phase element coefficient and φ is a dimensionless parameter related to the constant phase angle (constant phase element exponent). On smooth homogeneous electrodes, T becomes identical with pure capacitance as $\varphi = 1$ [34]. The most widely accepted explanation for the presence of this distributed element and appearance of depressed semicircles in Nyquist plots is microscopic roughness, which causes an inhomogeneous distribution in the solution resistance and in the double-layer capacitance [35].

An important theoretical model for the impedance response of a porous intercalating electrode has been established previously [30]. After that, the created model further theoretically developed for the lithium intercalation in a single particle as well as composite electrodes [36]. According to these works, two important parameters which affect the impedance response of the intercalating electrodes are the conductivity of both the electrolyte solution and the solid host material (electronic and ionic conductivities of solid-phase and the ionic conductivity of the solution-phase in the porous space between the particles denoted, respectively, as σ and κ). The effect of small values of κ and σ is known in terms of Ohmic potential drops in the pores filled with the electrolyte and in the solid-phase. This causes a high-frequency semicircle related to the combination of the charge transfer process and a typical low-frequency impedance response that reflects distribution elements to be seen, and the double layer capacitance to be squashed [30]. This particular type of dispersion of the capacitance of porous intercalating electrodes is related to coupling of interfacial and bulk quantities [37]. Along this line, in the Nyquist diagrams represented here, the squashed semicircle at high frequencies

which modeled for the intercalating electrodes is observed experimentally and is a result of a limitation in the value of κ and/or σ.

The charge-transfer resistance (R_{ct}) of the electrode reaction (Co(IV)/Co(III) redox transition) is the only circuit element that has a simple physical meaning describing how fast the rate of electron injection during intercalation/deintercalation changes with the electrode potential, while the other parameters are kept constant. The best equivalent circuit that fulfills the impedance characteristics of the whole intercalation process is shown in Scheme 1. This circuit was fitted to the experimental results using a non-linear least-square fit. In this circuit, R_s, R_{ct}, and CPE_{dl} characterize the high-frequency response and represent solution resistance, charge transfer resistance and double layer capacitance, respectively. Parallel combination of CPE_1 and R_1 characterizes the medium-frequency response and W_o and C_{int} characterize the low-frequency response indicating lithium ion diffusion and occupation, respectively. In Fig. 8, the symbols represent experimental data and the continuous lines were drawn using the values of the circuit elements obtained by fitting. The values of the equivalent circuit elements obtained by fitting and the corresponding errors are presented in Table 1. The good agreement between the fitted and experimental curves (which is also confirmed by the low numerical errors of the fitted values, Table 1) in the high frequency range (Fig. 8) led the R_{ct}, φ, and T values at different dc-offset potentials to be estimated. These values were plotted as a function of dc-offset potential and are shown in Fig. 9. φ remains almost constant for different dc-offset potentials at a value of 0.68. The value of T can be directly attributed to the double layer capacitance because the value of φ is constant at different dc-offset potentials. The value of the double layer capacitance is high at two potential edges of the intercalation/deintercalation processes. At the beginning of deintercalation (fully discharged state), the double layer capacitance is high because the charge accumulation occurs before the starting the faradaic process. Then, it suddenly decreases to a minimum value due to occurring of the deintercalation process. Then, it remains almost constant and reaches to a maximum value again at fully charged state. The value R_{ct} has the lowest value at high dc-offset potentials and remains almost constant in this potential range. Then, it increases upon decreasing the dc-offset potential. This behavior has been related to the surface defects that exist in the electroreactive nanoparticles [9]. During the redox process of the nanoparticles, the surface defects in the nanoparticles react firstly with a high rate (a low R_{ct}) and then, the bulk of the particles participates [9]. These surface defects present equal accessibility of the electroreactive sites on the first atomic layer of the nanoparticles, therefore, no initial variation in R_{ct} was observed [9]. After consumption of these defective sites, the reaction propagated deeper into the bulk of the nanoparticles; the reaction was carried out more difficultly and hence R_{ct} increases. From the variation of the value of R_{ct} in the pure charge transfer region, the exchange current density for the redox process of Co(IV)/Co(III) can be obtained using [22]:

$$R_{ct} = RT/nFi_0 \tag{9}$$

where n is the number of exchanged electrons, i_0 is the exchange current density and the other parameters have their usual meaning. The value of exchange current density was obtained as 5.30×10^{-3} A cm^{-2}. This value is higher than that reported elsewhere for the Co(IV)/Co(III) transition related to the lithium intercalation process in nonaqueous solutions [38]. From the value of exchange current density and the following equation [22],

$$i_0 = nFAk^0C^*_{Li} \tag{10}$$

the standard rate constant, k^0, for the faradaic reaction of Co(IV)/Co(III) during lithium intercalation was obtained as 3.38×10^{-5} cm s^{-1}.

At medium frequencies, an arc appeared in the Nyquist diagrams. This arc is characterized by a combination of a constant phase element and a resistance in parallel (CPE_1 and R_1 in Scheme 1) and is also a consequence of the limitation in the value of κ and/or σ (vide supra) [30, 36]. It should be noted that (any limitation in) the values of σ and κ affect the impedance response, when the redox reaction start to be occurring. Therefore, in the equivalent circuit represented in Scheme 1, R_{ct} and CPE_1–R_1 are placed in series.

The total impedance of the mixed particle porous electrode is represented as [30, 36, 39, 40]:

$$Z_{tot} = [r/(\sigma+\kappa)]\{1 + [2 + ((\sigma^2+\kappa^2)/\sigma\kappa))\cosh\zeta]/(\zeta\sinh\zeta)\} \tag{11}$$

with

$$\zeta = r[(\sigma+\kappa)\chi/\sigma\kappa Z_1]^{0.5} \tag{12}$$

and

$$Z_1 = (R_{ct} + Z_{diff})/[1 + j\omega C_{dl}(R_{ct} + Z_{diff})] \tag{13}$$

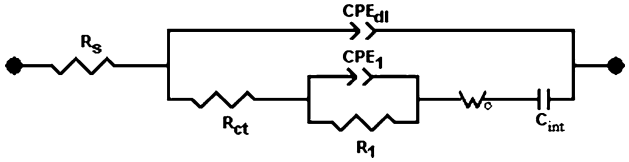

Scheme 1 The equivalent circuit that fulfilled the impedance spectra represented in Fig. 8

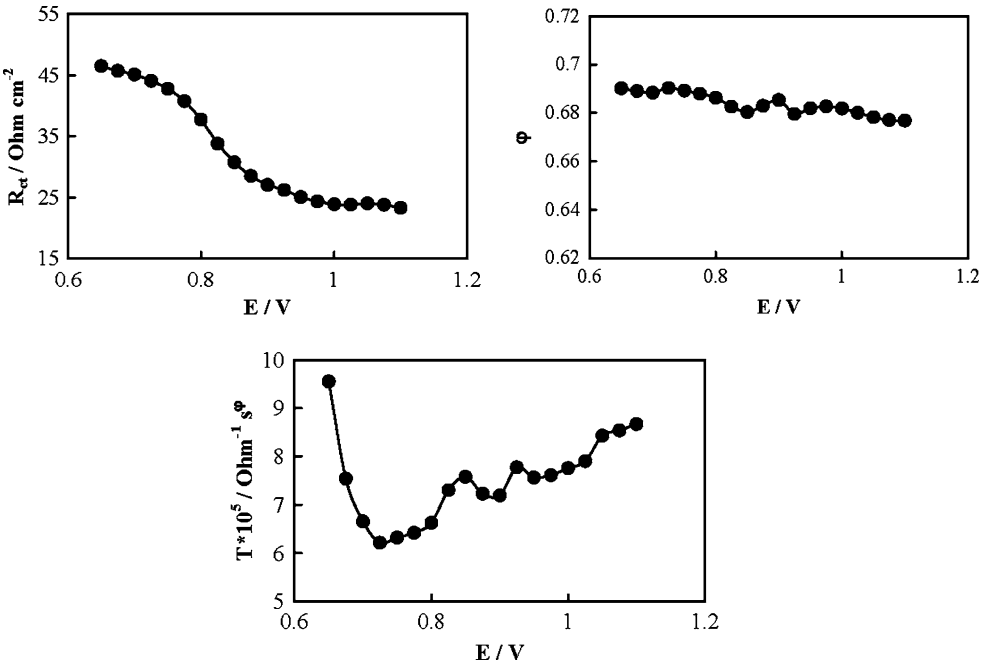

Fig. 9 Variations of R_{ct}, φ, and T on dc-offset potential. The data derived from Nyquist diagrams represented in Fig. 8

while

$$Z_{diff} = Z_{FLW} + C_{int} \tag{14}$$

and

$$Z_{FLW} = R_{FLW}\left\{ctnh(j\omega R_{FLW}C_{FLW})^{0.5}/(j\omega R_{FLW}C_{FLW})^{0.5}\right\} \tag{15}$$

where r is the nanoparticles radius, χ is the surface area to the volume ratio, Z_{FLW} is a finite length Warburg impedance, R_{FLW} analogizes the resistance of the diffusion of a species through a finite length, C_{FLW} describes the capacitance of the finite space, and C_{int} characterizes lithium ion occupation in the lattice sites. In Eq. (15), Z_{FLW} is the impedance of the one-dimensional diffusion of a particle, which is completely analogous to wave transmission in a finite-length RC transmission line [34]. Based on this impedance equation, finite values of κ and/or σ cause the appearance of both a squashed semicircle with an approximate unit slope in the limit of very high frequencies (which is due to the distributed character of the impedance at these finite values rather than to a semi-infinite diffusion [30]) and an arc in the middle frequencies.

The impedance response at low frequencies was comprised two individual time constants of diffusion process of lithium ion in the finite-space electrode material and the capacitive behavior of the characteristic response of a finite blocked diffusion through the electrode (lithium ion occupation in intercalated sites) during the intercalation/deintercalation (Eq. 15). In Eq. (15) [7, 34, 39, 40],

$$R_{FLW}C_{FLW} = \tau_d = r^2/D_{Li} \tag{16}$$

It should be noted that the active mass of the working electrode comprised nanoparticles of average radius, r. In such electrode, lithium ion diffusion occurs in the direction parallel to the electrode substrate, and the radius of the particles is the true diffusion length [39–41]. Here, the impedance of the electrode process in low-frequency range was modeled by a series combination of a W_o and C_{int}. Such combination causes that diffusion time constant to be independent of the active material thickness and it to be dependent on the radius of the intercalating particles. C_{int} is affected by the active materials thickness and any change in the electrode thickness, while r remains constant, causes only C_{int} to be changed [41]. Just for this reason, in the chronoamperometric studies, we used the electrode thickness as the diffusion length, while in the impedance measurements, the diffusion thickness was assumed to be the nanoparticles radius. The values of the electrical element components of the low-frequency response (τ_d) were obtained by a fitting procedure and are reported in Table 1. Using Eq. (16) and the values of τ_d, the values of D_{Li} in the nanoparticles of $LiCoO_2$ at each individual dc-offset potential were obtained and are reported in Table 1. D_{Li} is potential-dependent and changes smoothly. D_{Li} represents a minimum at 750 mV. Interestingly, this minimum value, which obtained from the Nyquist diagram recorded at dc-offset potential equal to the cathodic peak of cyclic voltammogram, is almost equal to that obtained from CV. Similar behavior for the dependency of solid state diffusion coefficient of lithium ion on the electrode potential has been reported elsewhere [21, 42, 43]. Appearance of a minimum in the dependency of D_{Li} on dc-offset potential has

been discussed based on different explanations. Barker et al. [42] related this minimum to the Li–Li ionic coulombic repulsions within each structural site in the host lattice. Prosini et al. [43] related this minimum to the strong attractive interactions between the lithium ions and the host lattice. Zhang et al. [32] related this minimum to the severe structural change and phase transformation of the host lattice during and also to the temporary strong Li-host lattice binding.

4 Conclusion

Nanoparticles of $LiCoO_2$ were prepared by a new process using citrate as fuel and metal acetates as the source of metal ions. The electron microscopy investigations indicated that the prepared cathodic materials have spherical shape with mean diameter of about 100 nm. Structural analysis using X-ray powder diffraction showed that synthesized $LiCoO_2$ nanoparticles were of good crystallinity, which was further confirmed by electrochemical experiments. The kinetic parameters of the intercalation were studied by means of CV and potential step CA. Lithium ion diffusion coefficient was determined by analyzing the data of the CV as well as CA measurements. Three different kinetic regions were differentiated from CA data analysis corresponding to the separate steps of the entire intercalation process. A careful interpretation of the impedance data obtained at different dc-offset potentials allowed the separation of different dominated processes.

Acknowledgments We would like to thank the Iran National Science Foundation (INSF) and the Research Councils of Islamic Azad University and K. N. Toosi University of Technology for supporting this research.

References

1. Wang GJ, Qu QT, Wang B, Shi Y, Tian S, Wu YP, Holze R (2009) Electrochim Acta 54:1199
2. Liu XH, Saito T, Doi T, Okada S, Yamaki J (2009) J Power Sources 189:706
3. Ruffo R, Wessells C, Huggins RA, Cui Y (2009) Electrochem Commun 11:247
4. Wang GJ, Zhao NH, Yang LC, Wu YP, Wu HQ, Holze R (2007) Electrochim Acta 52:4911
5. Chu A, Braatz P (2002) J Power Sources 112:236
6. Kim MG, Cho J (2009) Adv Funct Mater 19:1497
7. Heli H, Yadegari H (2010) Electrochim Acta 55:2139
8. Choy JH, Kim YI, Campet G, Portier J, Huong PV (1999) J Solid State Chem 142:368
9. Quintin M, Devos O, Delville MH, Campet G (2006) Electrochim Acta 51:6426
10. Linden D, Reddy TB (2002) Handbook of batteries, 3rd edn. McGraw-Hill Inc., New York
11. Sun YK (1999) J Power Sources 83:223
12. Choi KY, Kima KD, Yang JW (2006) J Mater Process Technol 171:118
13. Boyle TJ, Ingersoll D, Alam TM, Tafoya CJ, Rodriguez MA, Vanheusden K, Doughty DH (1998) Chem Mater 10:2270
14. Chiang YM, Jang YI, Wang H, Huang B, Sadoway DR, Ye P (1998) J Electrochem Soc 145:887
15. Striebel KA, Deng CZ, Wen SJ, Cairns EJ (1996) J Electrochem Soc 143:1821
16. Dokko K, Mohamedi M, Fujita Y, Itoh T, Nishizawa M, Umeda M, Uchida I (1996) J Electrochem Soc 148:A422
17. Wang G, Fu L, Zhao N, Yang L, Wu Y, Wu H (2007) Angew Chem 46:295
18. Cullity BD (1978) Elements of X-ray diffraction, 2nd edn. Addison-Wesley, Reading
19. Johnston WD, Heikes RR, Sestrich D (1958) J Phys Chem Solids 7:1
20. Yu Y, Shui JL, Jin Y, Chen CH (2006) Electrochim Acta 51:3292
21. Liao CL, Lee YH, Fung KZ (2007) J Alloys Compd 436:303
22. Bard AJ, Faulkner LR (2001) Electrochemical methods. Wiley, New York
23. Chen L-C, Ho K-C (2001) J Electrochem Soc 148:E282
24. Levi MD, Salitra G, Markovsky B, Teller H, Aurbach D, Heider U, Heider L (1999) J Electrochem Soc 146:1279
25. Prosini PP, Lisi M, Zane D, Pasquali M (2002) Solid State Ionics 148:45
26. Levi MD, Aurbach D (1997) J Phys Chem B 101:4641
27. Heli H, Jabbari A, Zarghan M, Moosavi-Movahedi AA (2009) Sens Actuators B 140:245
28. Levi MD, Levi EA, Aurbach D (1997) J Electroanal Chem 421:89
29. Das SR, Majumder SB, Katiyar RS (2005) J Power Sources 139:261
30. Meyers JP, Doyle M, Darling RM, Newman J (2000) J Electrochem Soc 147:2930
31. Wakihara M, Yamamoto O (1998) Lithium ion batteries: fundamentals and performance. Wiley-VCH, Tokyo
32. Zhang J, He P, Xia Y (2008) J Electroanal Chem 624:161
33. Funabiki A, Inaba M, Ogumi Z, Yoasa S, Otsuji J, Tasaka A (1998) J Electrochem Soc 145:172
34. Barsoukov E, Macdonald JR (2005) Impedance spectroscopy. Wiley, Hoboken, NJ
35. Maritan A, Toigo F (1990) Electrochim Acta 35:141
36. Levi MD, Aurbach D (2004) J Phys Chem B 108:11693
37. Pajkossy T (1994) J Electroanal Chem 364:111
38. Zhang Q, Guo Q, White RE (2007) J Power Sources 165:427
39. Levi MD, Aurbach D (1999) Electrochim Acta 45:167
40. Aurbach D, Levi MD, Levi E, Teller H, Markovsky B, Salitra G, Heider U, Heider L (1998) J Electrochem Soc 145:3024
41. Levi MD, Lu Z, Aurbach D (2001) Solid State Ionics 143:309
42. Barker J, Pynenburg R, Koksbang R (1994) J Power Sources 52:185
43. Prosini PP, Lisi M, Zane D, Pasquali M (2002) Solid State Ionics 148:45